Role of body stiffness in undulatory swimming: Insights from robotic and computational models

Eric D. Tytell[*]

Department of Biology, Tufts University, Medford, Massachusetts 02155, USA

Megan C. Leftwich

Department of Mechanical and Aerospace Engineering, George Washington University, Washington, DC 20052, USA

Chia-Yu Hsu

Department of Applied Mathematics, Feng Chia University, Taiwan

Boyce E. Griffith

Department of Mathematics and Department of Biomedical Engineering, University of North Carolina, Chapel Hill, North Carolina 27599, USA

Avis H. Cohen

Institute for Systems Research and Department of Biology, University of Maryland, College Park, Maryland 20742, USA

Alexander J. Smits

Department of Mechanical and Aerospace Engineering, Princeton University, Princeton, New Jersey 08544, USA

Christina Hamlet[†] and Lisa J. Fauci

Department of Mathematics and Center for Computational Science, Tulane University, New Orleans, Louisiana 70118, USA

In an effort to understand the locomotion dynamics of a simple vertebrate, the lamprey, both physical and computational models have been developed. A key feature of these models is the ability to vary the passive stiffness of portions of the swimmer, focusing on highly flexible models similar in material properties to lampreys and other anguilliform fishes. The physical model is a robotic lampreylike swimmer that is actuated along most of its length but has passively flexible tails of different stiffnesses. The computational model is a two-dimensional model that captures fluid-structure interactions using an immersed boundary framework. This simulated lamprey is passively flexible throughout its length and is also actuated along most of its length by the activation of muscle forces. Although the three-dimensional robot and the two-dimensional computational swimmer are such different constructs, we demonstrate that the wake structures generated by these models share many features and we examine how flexibility affects these features. Both models produce wakes with two or more same-sign vortices shed each time the tail changes direction (a "2P" or higher-order wake). In general, wakes become less coherent as tail flexibility increases. We examine the pressure distribution near the tail tip and the timing of vortex formation in both cases and find good agreement. Because we include flexibility, we are able to estimate resonant frequencies for several of the robotic and computational swimmers. We find that

---

[*]eric.tytell@tufts.edu; http://ase.tufts.edu/biology/faculty/tytell/

[†]Present address: Department of Mathematics, Bucknell University, Lewisburg, PA 17837, USA.

actuation at the resonant frequency dramatically increases the distance traveled per tail-beat cycle with only a small increase in the lost kinetic energy in the wake, suggesting that the resonant swimmers are more efficient.

I. INTRODUCTION

When fish swim, their bodies bend because of internal muscle forces, but also because of external forces from the environment. These two forces are coupled together by the stiffness, damping, and other passive mechanical properties of the fish's body. The motion that we observe is a delicate balance of these internal and external forces, filtered by the body mechanics [1]. Some fish are stiffer than others [2]; some fish have more internal damping than others [3,4]. The impact of these differences in material properties is not known.

Even though the body's material properties most likely have a strong effect on swimming performance, it is extremely difficult to use animal experiments to identify its role. While one species of fish may be stiffer than another, they also typically differ in numerous other ways, such as the anatomy of the muscle and skeleton and the way they activate their muscles during swimming. Instead, computational or robotic models offer a more controlled way to separate the different contributions of muscle activation patterns, body mechanics, and overall anatomy (e.g., [5,6]).

Our recent computational simulations of lamprey swimming [7,8] showed that stiffer swimmers accelerate faster but use more energy than more flexible swimmers, as long as the peak muscle force increases or decreases to match the body stiffness. Fluid-mechanical resonance may explain some of these differences. Quinn *et al.* [9] and Alben [10] found that flexible flapping or undulating panels can have multiple peaks in thrust or efficiency that depend on a set of nonlinear resonant interactions between the fluid and the body. In our previous work [11], by changing the stiffness but keeping the activation frequency constant, we were changing how close the system was to one of the resonant interactions.

In that study, we did not examine the fluid dynamic mechanisms underlying the performance differences. How does the wake structure correlate with swimming performance? When an animal produces a more coherent wake, we expect that it should swim more efficiently [12], but at the same time, differently organized wakes can result in similar swimming efficiency [13]. We might expect there to be an optimal stiffness for producing a coherent wake. Animals with very stiff bodies may be able to support a high velocity difference from one side of their body to the other, so that they could shed a strong shear layer into their wake; shear layers tend to be unstable [14], so such a stiff swimmer might produce an incoherent wake with many extra vortices. At the other end, very flexible bodies may deform too much during motion so that they do not shed individual, concentrated vortices [6]. At some intermediate stiffness, an animal might be able to produce an optimal coherent wake. Because the swimming is a resonant interaction with the fluid, though, the wake will also depend on the oscillation frequency.

The wake may also depend on the pressure distribution along the body. Fishes like eels and lampreys, which swim in an anguilliform mode with about one complete undulatory wave on their body [15], will have multiple regions of high and low pressure along their bodies [16,17]. These changes in pressure tend to correlate with a 2P wake structure [18], in which the swimmer sheds two pairs of vortices in each full tail beat [6,19]. Fishes like sunfish, which swim in a carangiform mode with much less than a full undulatory wave, will tend to have fewer changes in pressure along their bodies [20,21]. During steady forward swimming, such fishes generally produce 2S wakes, with two single vortices shed each cycle [15]. Here, we consider how the pressure fluctuations near the tail correspond to vortex shedding into the wake.

Both the computational and robotic swimmers that we examine are extremely flexible, compared to previous studies of flexible foils. There are not many measurements of the stiffness of fish bodies, but Long [22] measured eels to have a passive stiffness (Young's modulus E) as low as 0.39 MPa,

corresponding to a bending modulus EI of $1.6 \times 10^{-4} \mathrm{N\,m^2}$. Based on our experience, lamprey bodies are even more flexible than those of eels. Most previous studies of flexible propulsors, though, have used thin plastic foils with stiffness in the gigapascal range, which, because of their thinness, have bending moduli close to those of fish. For example, the most flexible panel in [9] had a modulus $EI = 0.6 \times 10^{-4} \mathrm{N\,m^2}$, but $E = 3.8\,\mathrm{GPa}$. To our knowledge, our study is the first to examine flexible propulsors that have material properties similar to those of fish and also match the relative thickness of their bodies.

To study these effects, we compare flow patterns from Leftwich *et al.* [6] around a robotic anguilliform swimmer with a flexible tail to those from Tytell *et al.* [7,11] around a two-dimensional computational simulation of a flexible anguilliform swimmer. Both models are simplifications. The robotic swimmer has a passively flexible tail, while the animal's muscles actively deform their bodies. The computational swimmer has active segments that approximate muscle running all the way down to its tail, like animals, but it is has only two spatial dimensions, while animals clearly have three. Nevertheless, we show that both models accurately capture important features of anguilliform swimming and serve as useful ways to study the interaction of material properties, muscle activation, and wake structure for swimming. Moreover, numerical convergence studies presented below show that high resolution detail of vortex formation in the computational algorithm is not necessary to accurately resolve the coupled fluid-body interaction. Based on these robotic and computational models, we investigate the role of flexibility in both wake formation and swimming performance.

II. METHODS

A. Methods for simulations

Tytell *et al.* [7] completed two-dimensional simulations of anguilliform swimming using an adaptive mesh immersed boundary method (IBAMR) [23,24]. These simulations differ from much previous work in that the motion of the swimmer is not prescribed. The swimming motion instead is the result of the interaction between the fluid, described by the Navier-Stokes equations, and a body model that describes both the passive elasticity and the active muscle contraction for a lamprey. The body is constructed from three filaments (a "backbone" and left and right sides), which are connected by a network of elastic filaments that approximate the geometry of serial blocks of muscle in fishes, called myomeres [25]. Internal filaments are Hookean springs, and resist both compression and extension. Filaments along the left and right sides only resist extension, like collagen fibers. Additionally, left and right side segments produce active forces, which are described by a Hill-type muscle model, after Williams *et al.* [26] and Hamlet *et al.* [27].

Body stiffness was altered by changing the stiffness of the passive springs that connect the filaments. An effective Young's modulus was estimated by bending the body through a set of known angles and calculating the energy stored in the springs [28]. At the same time, the maximum muscle force was increased or decreased to match the change in body stiffness; this produced swimmers of different stiffness that swam with similar tail-beat amplitude.

We prescribed a traveling wave of activation with a defined period (usually 1s) and one full wave on the body. This wave activated the muscle, which produced force, bending the body and interacting with the fluid. The swimmer was started from rest with a straight body and accelerated until it reached a steady swimming speed.

Convergence testing

We checked to make sure that the parameters of the adaptive mesh algorithm did not affect the computed motion of the swimmer. The overall motion was very robust to large changes in these parameters. This algorithm [23] adaptively increases the grid resolutions in areas with high vorticity or close to the material points of the swimmer. Two parameters control the adaptive mesh. First, the resolution doubles each time the vorticity changes by greater than (1) a vorticity threshold parameter,
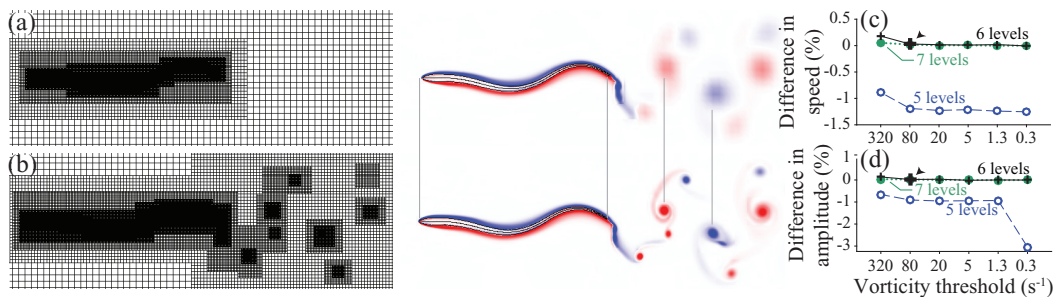
FIG. 1. Convergence tests of the adaptive mesh algorithm. Computational meshes and vorticity for (a) five refinement levels, vorticity threshold $320\,\mathrm{s}^{-1}$, and (b) six refinement levels, vorticity threshold $80\,\mathrm{s}^{-1}$. Percent differences in (c) swimming speed and (d) tail amplitude for different vorticity thresholds and levels of refinement.

up to (2) a maximum number of refinement steps. We tested how these two adaptive mesh parameters would affect the overall motion of the swimmer.

Figure 1 shows the results of testing with three different maximum grid refinement levels (five, six, or seven levels) and six thresholds for vorticity (from 5 to $320\,\mathrm{s}^{-1}$). The higher the vorticity threshold, the less often the resolution will increase. At the lowest refinement and the highest vorticity threshold, the adaptively refined Cartesian grid had on the order of 5×10^4 grid cells, whereas at the highest refinement and tightest vorticity threshold, the number of grid cells was approximately 5×10^6. Although the wake in Fig. 1(a) is very smoothed and poorly resolved, the body shape and swimming velocity are not very much different from the more highly resolved case [Fig. 1(b)]. Additionally, as long as there were at least six levels of refinement, there were negligible differences in the emergent properties of the coupled fluid-body interaction, such as the overall swimming speed [Fig. 1(c)] and tail-beat amplitude [Fig. 1(d)]. For that reason, all of the simulations here we performed with these intermediate parameters [indicated by an arrowhead in Figs. 1(c) and 1(d)].

B. Methods for robotic experiments

The robotic platform used in this work is a modification of that used by Hultmark *et al.* [29] and the same as that used by Leftwich and Smits [16] and Leftwich *et al.* [6]. It consists of 11 servomotors attached in alternating pairs. Each motor is controlled by a BasicX Stamp microcontroller (Parallax, Inc., Rocklin, CA, USA) that is programed to replicate the growing, traveling sine wave of anguilliform swimming. The motors and controller for the robot are shown in Fig. 3(c) at the top of the panel. The motion of the robot is based on the work of Tytell and Lauder [19] and detailed in Ref. [29]. The motors and controller shown in Fig. 3(c) were covered in a custom-made latex skin to isolate them from the water. Swimming speed and flow data were taken with three passively flexible tails ($E = 0.12, 0.17,$ and 0.23 MPa, corresponding to bending moduli $EI = 1.0 \times 10^{-4}, 1.4 \times 10^{-4},$ and $1.9 \times 10^{-4}\mathrm{N}\,\mathrm{m}^2$). These tails are geometrically similar to the silver lamprey (*Ichthyomyzon unicuspis*) and cast out of flexible PVC gel (M-F Manufacturing Co., Fort Worth, TX, USA). A plastic insert in the center of the flexible tail controls the degree of flexibility of each tail.

The experiments were conducted in a closed loop, free surface water channel with a test section that is 0.46 m wide, 0.3 m deep, and 2.5 m long. One honeycomb and three screens sit upstream of the 5:1 contraction. The anterior part of the robot was held in the test section at mid-depth by a frame mounted on an air-bearing sled free to move in the streamwise direction. Waves were eliminated by mounting a clear acrylic plate at the surface. Free swimming speeds were determined based on the water speed in the tunnel when the robot did not move in the streamwise direction while activated.

The flow field generated by the steadily swimming robotic lamprey was measured in the horizontal midplane of its wake using particle image velocimetry (PIV). The flow was seeded with silver coated

hollow ceramic spheres with a diameter of 100 μm and an average specific gravity of 1.01 (Potters Industries Inc. Conduct-O-Fil AGSL-150-30 TRD). A Spectra Physics 2020 Argon laser, wavelength of 490 nm (Newport Corporation, Mountain View, CA, USA), was then used to create a light sheet with an optical fiber delivery system and a Powell lens (Oz Optics Ltd., Ottawa, ON, Canada). The sheet thickness was typically 1.5 mm ($1/e$ thickness). The sheet was oriented parallel to the robot, in the midplane of the swimming robot. A Redlake MotionXtra HG-LE (IDT, Tallahassee, FL, USA) camera was mounted perpendicular to the laser sheet (above the water channel) and used to capture the image pairs with 8–10 ms between images. Pairs were taken at 10 Hz. Image pairs were captured with a time delay of 8–11 ms between images. Ten image pairs were captured each second. Exposure times were typically 3 ms. The acquired image pairs were processed using an in-house PIV code (details of the code are presented in Ref. [30]). Interrogation windows of 32 pixels were used with 50% overlap between windows.

In addition to the velocity field, the fluctuating pressure signal on the surface of the swimming body and an actively bending but otherwise rigid tail was measured using a Validyne DP 15 (Validyne Engineering Corp in Northridge, CA, USA) differential pressure transducer. This was connected to a CD379 Validyne carrier demodulator, with a range of 0.85 to 1.4 kPa and an accuracy of $\pm0.05\%$ of the full scale deflection. Ten pressure ports were placed on the robotic lamprey. Four were located in the rigid part of the active tail, and six were imbedded into the latex skin that surrounds the robot. The transducer was connected to an NI USB-6212 data acquisition board (National Instruments, Austin, TX, USA) and computer.

C. Methods for data analysis

1. Scaling flexibility

The flexibility of the computational swimmer and the robot were scaled according to the analysis in Ref. [9] to produce a nondimensional effective flexibility

$$\Pi_1 = \left(\frac{\rho h l^5 f^2}{EI} \right)^{1/2},$$

(1)

where ρ is the fluid density, h is the average height of the swimmer, l is the length, EI is the bending modulus, and f is the tail-beat frequency. For the two-dimensional (2D) computational swimmer, we assume that h is equal to the average width.

2. Measuring the resonant frequency

For both robotic and computational models, we identified the mechanical resonant frequency of several of the models by oscillating them up and down in water and measuring the frequency that produced the highest amplitude motion. For the robot, this produced a clear resonant peak at 0.28 Hz for the 0.17 MPa tail. For the computational swimmer, the resonance was more complicated, with peaks at least at 0.5 and 1.5 Hz; see the discussion in Ref. [11]. However, we observed a clear maximum in tail-beat amplitude for the freely swimming model at 0.5 Hz and so we refer to this as the resonant frequency [11].

3. Material properties of the swimmers

Throughout this paper, we compare a robot with three different passive tails, one of which was also oscillated at its resonant frequency (Table I). The body anterior to the tail was moved actively using servomotors that matched a given wave form. The tails were shaped to match the shape of a lamprey's tail and were 20% of the total length of the robot (0.9 m). See [6,29] for more details on the robot. Similarly, we compare the computational swimmer with five different passive stiffnesses, one of which was oscillated at the resonant frequency (Table I). Different from the robot, in the

TABLE I. Parameters for robotic and computational experiments.

	E (MPa)	EI ($\times 10^{-5}\,\mathrm{N\,m^2}$)	Frequency (Hz)	Π_1
Robot	0.12	10	0.56	3.10
	0.17	14	0.56	3.61
	0.23	19	0.56	4.27
	0.17	14	0.28	1.81
CFD	0.59	0.21	1.0	6.63
	0.64	0.23	1.0	6.36
	0.76	0.26	1.0	5.87
	0.98	0.34	1.0	5.15
	1.06	0.37	1.0	4.96
	1.06	0.37	0.5	2.49

computational model, we adjusted the underlying material properties but kept active force generation along most of the entire length. See [7,11] for more details on the computational swimmer.

4. Phase averaging for experimental measurements

The velocity data from the PIV experiment and the pressure data, both obtained with the robotic lamprey, were phase averaged over 20 cycles of motion. For the PIV data, 10 velocity fields were measured per second. The robot was programed to have a period of motion of exactly 1.8 s per cycle. Therefore, images at the same cycle of motion (i.e., images 1, 19, 37, 55, etc.) were averaged to produce 18 velocity fields representing the entire cycle of motion. The same method was employed to determine the average pressure field throughout the cycle. However, the temporal resolution of the pressure transducer was significantly higher (1 kHz). Again, 20 cycles of motion were used to calculate the average pressure cycle.

5. Power calculations

We calculated a measure of efficiency for each swimmer by estimating the kinetic energy flux $\dot{K}$ (a measure of the wake power):

$$\dot{K} = \rho h \int_C \mathbf{u}^2 \mathbf{u} \cdot \mathbf{n}\,ds, \tag{2}$$

where ρ is the density of the fluid, h is the vertical height of the swimmer, $\mathbf{u}$ is the fluid velocity, $\mathbf{n}$ is the unit vector normal to the edge of the planar control area C, and ds is the distance along the edge of the control area. The wake power was scaled for each swimmer to produce a power coefficient C_K [31,32] by dividing by the power required to overcome drag:

$$C_K = \frac{\dot{K}}{0.5\rho S U^3}, \tag{3}$$

where S is the wetted surface area of the swimmer, and U is the mean swimming speed. Error on C_K was calculated for experimental measurements based on the standard deviation of the PIV measurements [33].

The $\dot{K}$ is the flux through a control volume containing the entire robot. The incoming velocity was fixed for each experiment and was assumed to be uniform. While the PIV data only encompass the left side of the wake, the full wake can be constructed by mirroring the data and offsetting it by one half of a cycle [labeled "mirrored" in Fig. 2(a)]. In this analysis, we neglect the contributions through the sides of the control volume upstream of the tail, for which there are no velocity data.
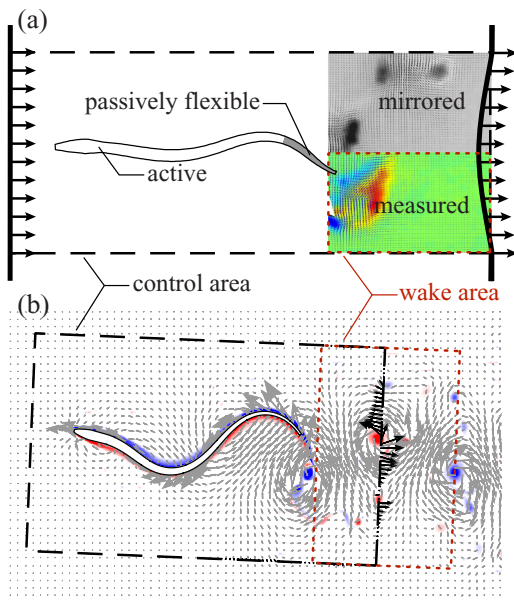
FIG. 2. Example control areas for the swimmers: (a) robot and (b) computational simulation. The boundary of the control area is given by a black dashed line, and the wake region for turbulence estimation is outlined with a red dashed line.

For the computational swimmer, we defined an area [Fig. 2(b)] surrounding the swimmer, moving at a constant velocity $\bar{\mathbf{U}}$ equal to the mean swimming speed and direction. Because of initial transients, the swimming direction was often angled relative to the horizontal axis, but the control area was aligned to the swimmer, as shown in Fig. 2(b). Fluid velocity was interpolated from the grid to the contour surrounding the area and integrated to estimate thrust, lateral forces, and wake power, all of which are defined per unit height.

6. Turbulence parameters

To assess the coherence and regularity of the wake, we estimated a phase-dependent turbulence intensity of the wake. First, we phase averaged the wake at 18 different phase values over at least three cycles and then computed the relative mean squared difference of the instantaneous fields with the phase averages:

$$I = \frac{1}{2}\left\langle \frac{(u - \overline{u_\phi})^2 + (v - \overline{v_\phi})^2}{\overline{u_\phi}^2 + \overline{v_\phi}^2} \right\rangle, \tag{4}$$

where $\overline{u_\phi}$ and $\overline{v_\phi}$ are the average mean components of velocity at a particular location and phase ϕ, and $\langle \cdot \rangle$ denotes an average over both space and phase. The value of I does depend on the number of cycles averaged, but the pattern relative to flexibility was very robust. Note that (u, v) includes the mean swimming speed U, even though it has been subtracted in figures showing wake flow patterns. For the robot, we used the measured wake region, which included half the wake laterally and approximately one spatial period behind the tail [Fig. 2(a)]. Error on I was calculated for experimental measurements based on the error of the PIV measurements [33]. For the computational swimmer, we used a domain in the wake from just behind the mean tail position to one full wake cycle (Uf, where U is the mean swimming speed and f is the tail-beat frequency) downstream [Fig. 2(b)].
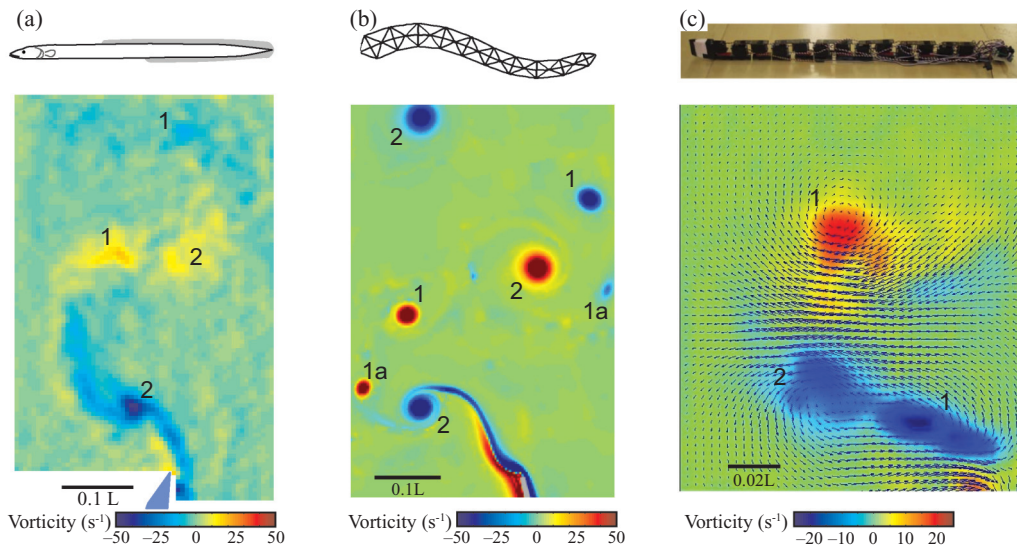
FIG. 3. Wakes of (a) a swimming eel, (b) the computational swimmer, and (c) the robotic swimmer all show the same overall 2P wake structure. The tails of the swimmers are at the bottom of each panel. Data replotted from [7,19,29].

III. RESULTS AND DISCUSSION

A. Wake structures of the robot, the simulations, and living eels

All of the swimmers shed a wake with two pairs of primary vortices shed per cycle, and the basic structures match qualitatively (Fig. 3). In both the wake of the living eel (swimming at 1.5 lengths s^{-1}; [19]) and the robotic swimmer [29] [shown in Figs. 3(a) and 3(c), respectively] a strong, repeatable pair of similar strength vortices was shed each half cycle—a two pair (2P) wake structure [34]. The underlying wake structure for the computational swimmer is also a 2P structure [7]. However, in Fig. 3(b) we see that the primary vortex (1) often splits a second time (1a). Thus, each cycle the computational swimmer produces a primary and secondary vortex of similar strength, as well as a weak tertiary vortex. In no case did any of the swimmers produce a 2S wake, although the wake of accelerating eels becomes closer to a 2S pattern [35]. Previous studies have observed that flapping propulsors tend to produce 2P wakes when Strouhal number St is high [36,37], as it is for our swimmers (St $\geqslant$ 0.5 for all cases). Using a more fishlike geometry, Borazjani and Sotiropoulos [38] also found that lamprey shaped swimmers almost always produced 2P wakes, except when the Strouhal number was 0.2 or less.

Both the computational and robotic swimmers that generated the data presented in Figs. 3(b) and 3(c) had active tails. The muscles or motors extended to the end of the swimming body. The coherence and repeatability of the wake degraded as the tail became more passive. Additionally, the presence of higher-order wake patterns was more prominent in these cases. While the main structure generally remained a 2P wake, it was common to see distinct structures in addition to the primary and secondary pairs. These structures were neither repeatable not predictable from cycle to cycle, but may contribute to the increase in the wake power for more flexible swimmers.

B. Very flexible swimmers swim slower, but resonance increases swimming speed

For very flexible swimmers (Young's modulus $E < 1$ MPa, which included all of the robotic swimmers and all but the least flexible computational swimmer; Table I), both computational and robotic, decreasing stiffness leads to decreasing swimming speed (Fig. 4). For both types of
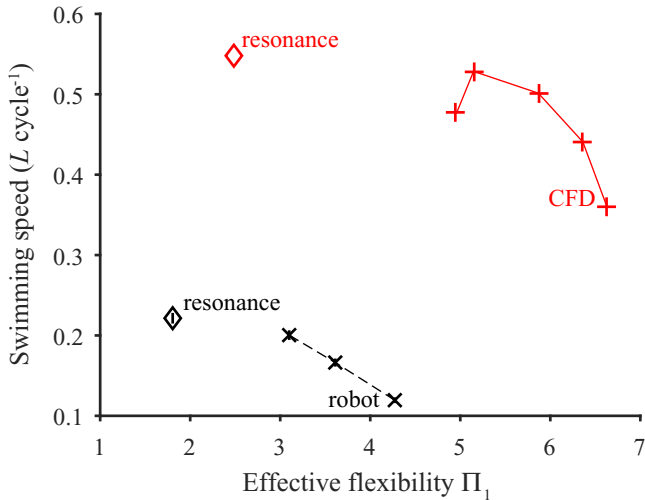
FIG. 4. Normalized swimming speed for robotic (black) and computational (red) swimmers of different stiffness, when oscillating at a constant frequency (dashed lines) and at a resonant frequency (diamonds). Error bars may be smaller than symbols.

swimmers, we adjusted the passive stiffness and then tuned the muscle force or motor power so that the overall tail-beat amplitude remained approximately the same. For the computational swimmer, doubling (or halving) the peak muscle force to match a doubling (or halving) of the body stiffness tended to preserve the overall amplitude [7]. For comparison, eels have a stiffness of approximately 0.39 MPa [22]. Under these conditions, increasing flexibility leads to decreasing swimming speed (Fig. 4). When the motion is determined by a balance of fluid forces and internal forces, as it is for the computational swimmer, there is an optimal stiffness for maximum swimming speed (Fig. 4, red points) at the same tail-beat frequency. For flexible bodies, like the robot tail, fluid-structure interactions can deform the body, reducing the transfer of momentum from the body to the water and lowering the swimming speed.

If the tail-beat frequency changes, mechanical resonance can improve the swimming speed. Oscillating at the resonant frequency decreases the effective flexibility [see Eq. (1)] and produces dramatic increases in the distance traveled per tail-beat cycle (red diamonds in Fig. 4). For both types of swimmer, the resonant frequency was lower than the frequency used in most of the tests; this means that the absolute swimming speed in ms^{-1} is lower for the resonant swimmers. But in each case, swimming at the resonant frequency is much more effective, traveling much farther during each tail beat than the nonresonant swimmers.

Quinn *et al.* [9] found a complex relationship between thrust force and stiffness for tethered flexible panels when they heave from side to side. They measured force and propulsive efficiency for foils with different stiffness, as they varied the flapping frequency and the oncoming flow speed. They found multiple distinct resonant peaks in thrust force as frequency varied. In general, however, at a given frequency, they found that more flexible foils produced lower forces than stiffer foils [9], matching our results. Similarly, numerical simulations of freely swimming foils in an inviscid fluid showed resonant peaks in swimming speed, but with speed decreasing on average as flexibility increased [39].

The mechanical resonant frequency of a flapping foil in water is not necessarily the frequency that produces the fastest swimming speed [40], but often the optimal frequency is close to the mechanical resonance. When both the robot and the computational swimmer used frequencies above the resonant frequency, they swam slower than when they used the resonant frequency. It is possible that even lower frequencies might have produced faster swimming, but we did not test those frequencies.
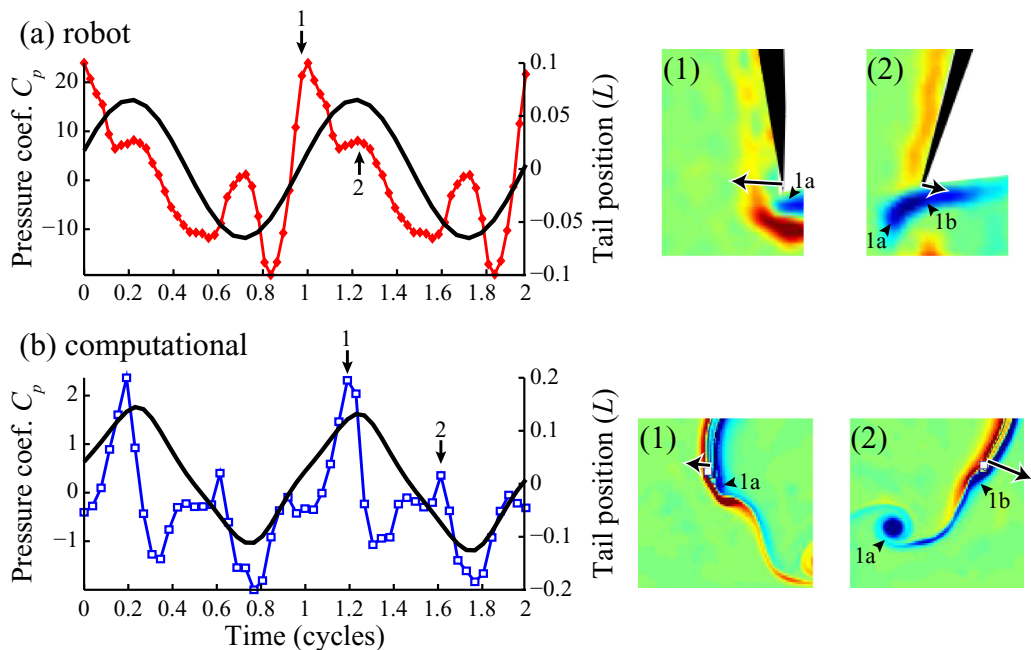
FIG. 5. Pressure traces and flow fields near the tail for the (a) robotic and (b) computational swimmers. Panels on the right show example wakes at the times labeled with arrows and the approximate tail velocity is shown with a gray arrow.

C. Pressure increases near the tail as vortices are shed

The fluctuations in pressure near the tail correspond to the timing of vortex shedding. Figure 5 shows the pressure coefficient C_p as a function of time for two full tail-beat cycles for both the robotic and computational swimmer. The pressure coefficient is defined as

$$C_p = \frac{p}{\frac{1}{2}\rho U^2},\tag{5}$$

where p is the pressure measured from the transducer as discussed in Sec. II B. In both cases, the pressure value used was taken from $0.98L$ from the head of the swimmer (very near the tip of the tail).

When C_p hits a local maximum (labeled with numbers), vortices are shed into the wake (right side). The global peak, labeled "1" in Figs. 5(a) and 5(b), comes just before the tail changes direction and begins moving away from the pressure port. This is just after the maximum acceleration of the tail at that location. The pressure takes over half the cycle (82% for the robotic swimmer and 60% for the computational swimmer) to reach its global minimum.

Using the velocity fields measured or computed, we can compare the pressure signal to the coherent structures present near the swimming surface. In Fig. 5 the panels on the right show the vorticity near the tail at the times marked in the figure. Panel (1) shows the velocity field at the global maximum of the pressure. We see that the large starting-stopping vortex that will form the primary vortex 1a from this half cycle has just detached from the tail. As this happens, the pressure rises dramatically, just before the peak labeled 1. This point occurs when the tail has just passed the midpoint of the robot and is moving to the left (indicated by the gray arrow). Point 2 is the second maximum—occurring just after the tail reaches its maximum amplitude and has changed directions. At this time, the pressure has decreased somewhat as the local boundary layer has weakened. These spatial and temporal fluctuations in the pressure gradients then change the local free-stream velocity,
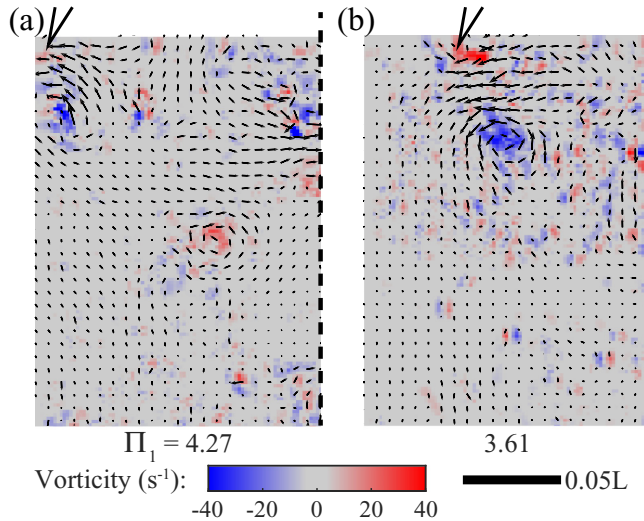
FIG. 6. Flow patterns in the wake of the robotic lamprey with (a) a very flexible tail and (b) a moderately stiff tail. The approximate position of the tail is shown at the top and the dashed line indicates the middle plane of symmetry.

which changes the local circulation. Ultimately, the time varying circulation establishes the strength of the trailing vortices shed into the wake.

D. Very flexible tails produce less repeatable wakes

For very flexible swimmers, increasing flexibility leads to increasingly disorganized wakes (Figs. 6 and 7). The phase-dependent turbulence intensity (Fig. 8) shows that, at a constant frequency, the wakes become less organized as flexibility increases, at least for very flexible swimmers ($E < 1$ MPa). Regardless of flexibility, the robot (Fig. 6) always produces a 2P wake, with two pairs of coherent structures that largely contain opposite signed vorticity. As the flexibility increases, the robot's wakes become far more chaotic: the structures have less concentrated vorticity and more often have patches of oppositely signed vorticity. This is seen in the differences between Figs. 6(a) and 6(b). While in both cases, a positive and negative vortex can be identified, the coherent, oppositely signed pair—the hallmark of the 2P wake—is clearly visible immediately downstream of the body for the moderately stiff tail [Fig. 6(b)]. The very flexible tail [Fig. 6(a)] produces a pair that is of unequal strength and inconsistent location in the wake.

For the computational swimmer (Fig. 7), very flexible swimmers also produce less coherent wakes, but the pattern is different: rather than shedding disorganized structures, the computational swimmer produces more vortices of alternating sign that are less repeatable [Fig. 7(a)]. For example, in Fig. 7(a), note the presence of small packets of vorticity near the vortex at the top of the panel; these do not tend to line up well with the black contours from the previous cycle. As in the case of the robot, the wake of the computational swimmer begins to regain coherence as the tail is stiffened [Figs. 7(b) and 7(c)]. Fewer structures are found in each cycle, and the vortex locations are more consistent from cycle to cycle. This can be seen in the greater overlap between the colored vortices and the black outlines in Fig. 7(c), compared to Fig. 7(a) particularly. Because the computational swimmer is 2D, it almost always produces a shear layer off the tip of the tail that then rolls up into additional vortices in the wake. An equivalent three-dimensional (3D) swimmer would most likely produce a less intense shear layer, because flow could move vertically around the tail, rather than just being shed off in the horizontal plane.
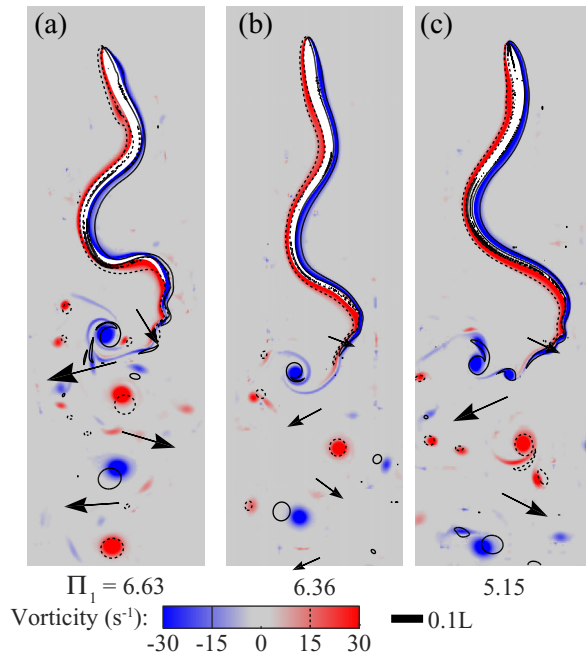
FIG. 7. Vorticity in the wake of the computational swimmer with (a) a very flexible body, (b) a moderately flexible body, and (c) a relatively stiff body. Vorticity in one cycle is shown in color, while vorticity contours from the previous cycle are overlaid in black.

Phase-dependent turbulence intensity follows the patterns seen in Figs. 6 and 7. For the robot, the swimmer with the stiffest tail has the lowest turbulence intensity and the highest swimming speed (black points in Figs. 4 and 8). For the simulation, the intermediate stiffnesses have the lowest turbulence intensity, but the stiffer swimmer, which has a somewhat less repeatable wake, swims faster (red points in Figs. 4 and 8). Resonance seems to increase the regularity of the wake, particularly for the robot, but since the resonant frequencies were much lower than the test frequencies shown in Fig. 8, the turbulence intensity results from resonant trials are not directly comparable and are therefore not shown.
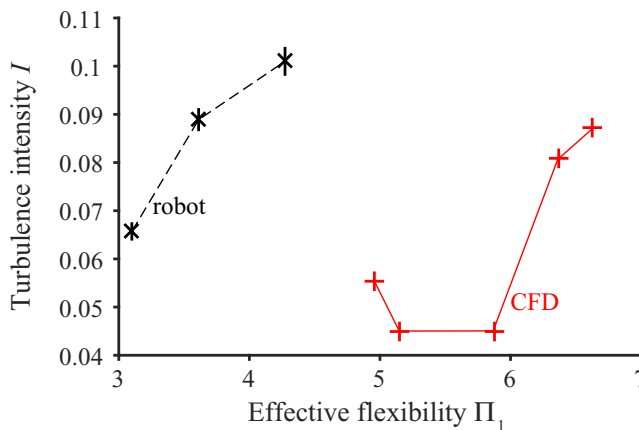
FIG. 8. Phase-dependent turbulence intensity for the robot (black) and computational swimmer (red).
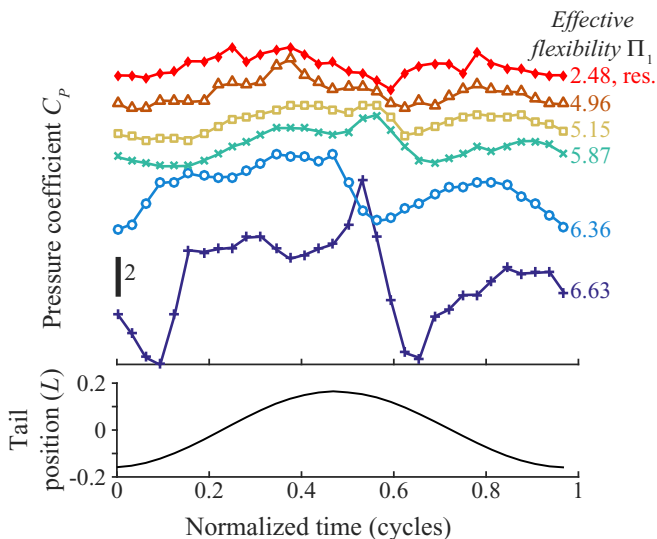
FIG. 9. Pressure coefficient near the tail tip and tail position for computational simulations with different stiffnesses. For visibility, the pressure traces have been offset from one another, arranged from the most flexible on the bottom to the stiffest on the top. The top (red) trace shows pressure from the 0.5Hz swimmer, which is at its resonant frequency.

For the computational swimmer, we were able to examine how the changes in pressure near the tail relate to the stiffness of the body and the coherence of the wake. Figure 9 shows that, for the two most flexible swimmers, the pressure varies over a higher range than for the stiffer swimmers ($E > 0.76$ MPa). For the stiffest swimmer ($E = 1.06$ MPa), the pressure tends to have small jumps, while at intermediate stiffness, the pressure varies both smoothly and over a smaller range. These swimmers also swim fastest (Fig. 4) and have wakes with lower turbulence intensity (Fig. 8). At an intermediate stiffness (0.98M Pa) we find that the pressure fluctuates the least. The intermediate swimmer also has the most coherent wake [Figs. 7(b) and 8]. The larger fluctuations in pressure for the high and low stiffness swimmers corresponds to increased vortex shedding and a less coherent wake [Figs. 7(a) and 7(c)].

E. Wake power

We find that more flexible swimmers dump relatively more kinetic energy into the wake than stiffer swimmers, resulting in a larger wake power coefficient (Fig. 10). This represents wasted energy, the portion of the overall energetic budget that does not help propel the animal forward, indicating that the more flexible swimmers are probably less efficient than the stiffer swimmers. Efficiency is difficult to assess during steady free swimming [31,32,41]. The total force on a swimmer, averaged over a cycle period, must be zero, because the swimmer is neither accelerating nor decelerating. For anguilliform swimmers like those studied here, the thrust and drag forces also balance fairly evenly along the body [41]. Thus, neither thrust nor drag can be measured directly, even for the computational swimmer. Various groups [42,43] have used different approximations for thrust or drag. In particular, Raspa *et al.* [43] found that thrust from elongated body theory matched the drag due to streamwise vortices shed along the top and bottom of a flapping plate. It is not clear, however, how this would apply to a 2D swimmer, which cannot shed these types of vortices. Instead, we use the wake power, a different measure of efficiency. Higher wake power indicates a less efficient swimmer [41].
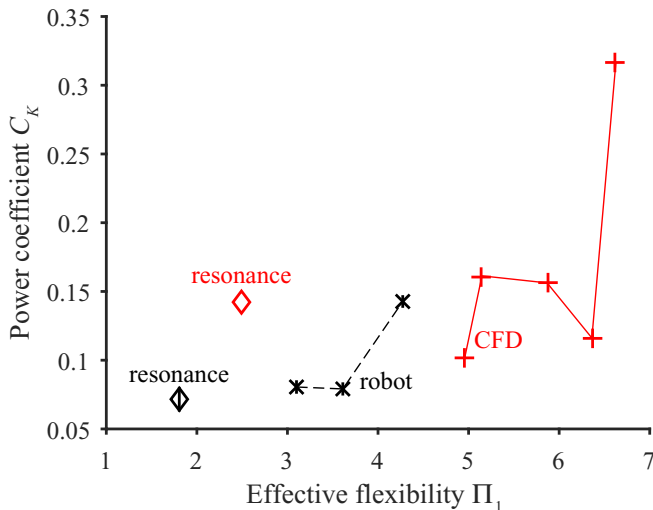
FIG. 10. Wake power coefficients for the robotic (black) and computational (red) swimmers with different effective flexibility.

In a previous paper [6], we used elongated body theory to estimate the mean thrust for the robot with flexible tails. We found that the thrust decreased as flexibility increased. Here, we find that the wake power coefficient increases with increasing flexibility (Fig. 10); together, the decrease in thrust and increase in wasted power show that efficiency drops dramatically as flexibility increases, for these very flexible swimmers. Other groups (e.g., [44,45]) have found that a passively flexible tail or trailing edge flap can increase swimming performance, but these studies used much stiffer materials.

The increase in wake power is largely due to an increase in the lateral velocities in the wake. Figures 6 and 7 show the wakes for the computational and robotic swimmers, with representative velocity vectors shown in the jet regions of the wake. Note that the lateral velocities are higher for the more flexible swimmers [Figs. 6(a) and 7(a), particularly], while the axial velocities are fairly similar.

Quinn *et al.* [9] found that maximum efficiency at resonant frequencies increased for flapping foils as they became more flexible, while we found that more flexible foils were less efficient. However, these results do not contradict ours, because the relationship was quite complex; depending on the flow speed and frequency, the efficiency could increase or decrease as stiffness changed [9].

IV. CONCLUSIONS

To understand the role of body stiffness in the swimming performance of fish, it is very challenging to study actual fish. Related species may differ in stiffness [2], but they often have many other differences. Instead, robotic and computational models offer a controlled way to analyze flow features and mechanics as a function of body flexibility [46]. While the models presented here are great simplifications of the true animal, they are not simple. The robotic model undulates its body to produce thrust, but its tail flexes passively in response to fluid forces. These interactions are still poorly understood. The computational model couples an actuated, elastic swimmer to the full Navier-Stokes equations, albeit in two dimensions. In order to characterize the bending modulus and the resonant frequency of the flexible components of each model, similar experiments that bent or oscillated the robot tail and the computational swimmer in a physical water tank or an *in silico* tank were performed. Even though the 3D robot and the 2D computational swimmer are such different constructs chosen to represent an anguilliform swimmer, we see excellent qualitative

agreement when comparing many metrics. In both, an active swimmer produces a 2P wake structure, and increasing flexibility decreases the wake coherence and increases the instances of spontaneous vortex shedding. The coefficient of pressure very near the tip of the tail in both cases contains three local maxima per cycle. These maxima are connected to vortex shedding at the tail and vorticity fields show this connection. Not surprisingly, the wake features of the 3D robot match those of a swimming eel more closely than the 2D computational swimmer.

---

[1] E. D. Tytell, P. Holmes, and A. H. Cohen, Spikes alone do not behavior make: Why neuroscience needs biomechanics, Curr. Opin. Neurobiol. **21**, 816 (2011).

[2] Y. Aleyev, *Nekton* (Junk, The Hague, 1977).

[3] J. H. Long, M. Koob-Emunds, B. Sinwell, and T. J. Koob, The notochord of hagfish *Myxine glutinosa*: Visco-elastic properties and mechanical functions during steady swimming, J. Exp. Biol. **205**, 3819 (2002).

[4] M. E. Porter, T. J. Koob, and A. P. Summers, The contribution of mineral to the material properties of vertebral cartilage from the smooth-hound shark *Mustelus californicus*, J. Exp. Biol. **210**, 3319 (2007).

[5] E. D. Tytell, I. Borazjani, F. Sotiropoulos, T. V. Baker, E. J. Anderson, and G. V. Lauder, Disentangling the functional roles of morphology and motion in the swimming of fish, Integr. Compar. Biol. **50**, 1140 (2010).

[6] M. C. Leftwich, E. D. Tytell, A. H. Cohen, and A. J. Smits, Wake structures behind a swimming robotic lamprey with a passively flexible tail, J. Exp. Biol. **215**, 416 (2012).

[7] E. D. Tytell, C. Hsu, T. L. Williams, A. H. Cohen, and L. J. Fauci, Interactions between internal forces, body stiffness, and fluid environment in a neuromechanical model of lamprey swimming, Proc. Natl. Acad. Sci. USA **107**, 19832 (2010).

[8] L. A. Miller, D. I. Goldman, T. L. Hedrick, E. D. Tytell, Z. J. Wang, J. Yen, and S. Alben, Using computational and mechanical models to study animal locomotion, Integr. Compar. Biol. **52**, 553 (2012).

[9] D. B. Quinn, G. V. Lauder, and A. J. Smits, Scaling the propulsive performance of heaving flexible panels, J. Fluid Mech. **738**, 250 (2014).

[10] S. Alben, Optimal flexibility of a flapping appendage in an inviscid fluid, J. Fluid Mech. **614**, 355 (2008).

[11] E. D. Tytell, C.-Y. Hsu, and L. J. Fauci, The role of mechanical resonance in the neural control of swimming in fishes, Zoology **117**, 48 (2014).

[12] G. S. Triantafyllou, M. S. Triantafyllou, and M. A. Grosenbaugh, Optimal thrust development in oscillating foils with application to fish propulsion, J. Fluids Struct. **7**, 205 (1993).

[13] D. B. Quinn, G. V. Lauder, and A. J. Smits, Maximizing the efficiency of a flexible propulsor using experimental optimization, J. Fluid Mech. **767**, 430 (2015).

[14] T. E. Faber, *Fluid Dynamics for Physicists* (Cambridge University Press, Cambridge, UK, 1995).

[15] G. V. Lauder and E. D. Tytell, Hydrodynamics of undulatory propulsion, in *Fish Biomechanics*, edited by R. E. Shadwick and G. V. Lauder (Academic Press, San Diego, CA, 2006), pp. 425–468.

[16] M. C. Leftwich and A. J. Smits, Thrust production by a mechanical swimming lamprey, Exp. Fluids **50**, 1349 (2011).

[17] B. J. Gemmell, S. P. Colin, J. H. Costello, and J. O. Dabiri, Suction-based propulsion as a basis for efficient animal swimming, Nat. Commun. **6**, 8790 (2015).

[18] M. M. Koochesfahani, Vortical patterns in the wake of an oscillating airfoil, AIAA J. **27**, 1200 (1989).

[19] E. D. Tytell and G. V. Lauder, The hydrodynamics of eel swimming. I. Wake structure, J. Exp. Biol. **207**, 1825 (2004).

[20] A. B. Dubois, G. A. Cavagna, and R. S. Fox, Pressure distribution on the body surface of swimming fish, J. Exp. Biol **60**, 581 (1974).

[21] M. A. Green and A. Smits, Effects of three-dimensionality on thrust production by a pitching panel, J. Fluid Mech. **615**, 211 (2008).

[22] J. H. Long, Muscles, elastic energy, and the dynamics of body stiffness in swimming eels, Am. Zool. **38**, 771 (1998).

[23] B. E. Griffith, R. D. Hornung, D. M. McQueen, and C. S. Peskin, An adaptive, formally second order accurate version of the immersed boundary method, J. Comput. Phys. **223**, 10 (2007).

[24] B. Griffith, An accurate and efficient method for the incompressible Navier-Stokes equations using the projection method as a preconditioner, J. Comput. Phys. **228**, 7565 (2009).

[25] Q. Bone, N. B. Marshall, and J. H. S. Blaxter, *Biology of Fishes*, 2nd ed. (Chapman and Hall, London, 1995).

[26] T. L. Williams, G. Bowtell, and N. A. Curtin, Predicting force generation by lamprey muscle during applied sinusoidal movement using a simple dynamic model, J. Exp. Biol. **201**, 869 (1998).

[27] C. Hamlet, L. J. Fauci, and E. D. Tytell, The effect of intrinsic muscular nonlinearities on the energetics of locomotion in a computational model of an anguilliform swimmer, J. Theor. Biol. **385**, 119 (2015).

[28] S. Lim and C. S. Peskin, Simulations of the whirling instability by the immersed boundary method, SIAM J. Sci. Comput. **25**, 2066 (2004).

[29] M. Hultmark, M. C. Leftwich, and A. Smits, Flowfield measurements in the wake of a robotic lamprey, Exp. Fluids **43**, 683 (2007).

[30] J. M. Jiménez, High Reynolds number flows about bodies of revolution (with application to submarines and torpedoes), Ph.D. thesis, Princeton University, 2007 (unpublished).

[31] W. W. Schultz and P. W. Webb, Power requirements of swimming: Do new methods resolve old questions? Integr. Compar. Biol. **42**, 1018 (2002).

[32] E. D. Tytell, The hydrodynamics of eel swimming. II. Effect of swimming speed, J. Exp. Biol. **207**, 3265 (2004).

[33] D. P. Hart, PIV error correction, Exp. Fluids **29**, 13 (2000).

[34] C. H. K. Williamson and A. Roshko, Vortex formation in the wake of an oscillating cylinder, J. Fluid Struct. **2**, 355 (1988).

[35] E. D. Tytell, Kinematics and hydrodynamics of linear acceleration in eels, *Anguilla rostrata*, Proc. R. Soc. London B **271**, 2535 (2004).

[36] H. Dai, H. Luo, P. J. S. A. Ferreira de Sousa, and J. F. Doyle, Thrust performance of a flexible low-aspect-ratio pitching plate, Phys. Fluids **24**, 101903 (2012).

[37] J. H. J. Buchholz and A. J. Smits, The wake structure and thrust performance of a rigid low-aspect-ratio pitching panel, J. Fluid Mech. **603**, 331 (2008).

[38] I. Borazjani and F. Sotiropoulos, On the role of form and kinematics on the hydrodynamics of self-propelled body/caudal fin swimming, J. Exp. Biol. **213**, 89 (2010).

[39] S. Alben, C. Witt, T. V. Baker, E. Anderson, and G. V. Lauder, Dynamics of freely swimming flexible foils, Phys. Fluids **24**, 051901 (2012).

[40] S. Ramananarivo, R. Godoy-Diana, and B. Thiria, Rather than resonance, flapping wing flyers may play on aerodynamics to improve performance, Proc. Natl. Acad. Sci. USA **108**, 5964 (2011).

[41] E. D. Tytell, Do trout swim better than eels? Challenges for estimating performance based on the wake of self-propelled bodies, Exp. Fluids **43**, 701 (2007).

[42] I. Borazjani and F. Sotiropoulos, Numerical investigation of the hydrodynamics of anguilliform swimming in the transitional and inertial flow regimes, J. Exp. Biol. **212**, 576 (2009).

[43] V. Raspa, S. Ramananarivo, B. Thiria, and R. Godoy-Diana, Vortex-induced drag and the role of aspect ratio in undulatory swimmers, Phys. Fluids **26**, 041701 (2014).

[44] A. Crespi, K. Karakasiliotis, A. Guignard, and A. J. Ijspeert, Salamandra Robotica II: An amphibious robot to study salamander-like swimming and walking gaits, IEEE Trans. Robot. **29**, 308 (2013).

[45] S. P. Colin, J. H. Costello, J. O. Dabiri, A. Villanueva, J. B. Blottman, B. J. Gemmell, and S. Priya, Biomimetic and live medusae reveal the mechanistic advantages of a flexible bell margin, PLoS ONE **7**, e48909 (2012).

[46] G. V. Lauder, J. Lim, R. Shelton, C. Witt, E. Anderson, and J. L. Tangorra, Robotic models for studying undulatory locomotion in fishes, Mar. Technol. Soc. J. **45**, 41 (2011).